Surface & Coatings Technology 205 (2011) 3378–3386

Contents lists available at ScienceDirect

Surface & Coatings Technology

journal homepage: www.elsevier.com/locate/surfcoat

Thermal fatigue resistance of plasma sprayed yttria-stabilised zirconia onto borided hot work tool steel, bonded with a NiCrAlY coating: Experiments and modelling

Pierre D'Ans *, Jean Dille, Marc Degrez

Université Libre de Bruxelles, Service Matières et Matériaux. 50, Avenue F.D. Roosevelt, CP194/3, 1050 Bruxelles, Belgium

ARTICLE INFO

Article history:
Received 1 September 2010
Accepted in revised form 23 November 2010
Available online 1 December 2010

Keywords:
Thermal fatigue
Coffin–Manson equation
Multi-layer
Aluminium diecasting
Plasma spray
Boriding

ABSTRACT

Repeated fast surface temperature transients can damage the materials and/or their surface treatments by thermal fatigue. This happens in aluminium diecasting devices. One conducted thermal fatigue tests with samples of hot work tool steel, respectively untreated, simply borided and protected by a multi-layer. In the last case, top coat is yttria stabilised zirconia (YSZ), followed by a nickel superalloy and then a borided layer (undercoat). The zirconia coating was applied with plasma spray. The multi-layer showed poor resistance during the thermal fatigue tests. Better understanding these tests and the resulting thermal fatigue observed on the treated materials was achieved by a lifetime model based on Coffin–Manson equations.

1. Introduction

A major wear mode of steel in the aluminium foundry industry is thermal fatigue, especially affecting diecasting dies. It also combines with intensive steel corrosion by molten aluminium (formation of intermetallic compounds or "soldering") and, sometimes, sliding wear, when extracting the moulded parts from the die [1,2].

On one hand, many surface treatments were studied to address at least one of these problems: nitriding [1,3–7] and shot peening [8] for thermal fatigue resistance; steel boriding [9–11], vanadium carbide diffusion layers [2], thin nitride PVD coatings [12–17] and thermally-sprayed boride coatings [18,19] mainly for corrosion resistance; oxide [20] or carbide [21] coatings for improved lubrication at high temperatures.

Since all these single treatments are not able to solve all the encountered problems individually, combining them was proposed. Most studied is a "duplex" treatment of nitriding with a PVD anticorrosive coating [4,14,22–25]. Another way of reducing thermal fatigue is lowering the thermal flux reaching the substrate. This is obtained combining an anticorrosive layer and a thermal barrier coating. Generally, additional bond coats ought to be inserted in this stacking [26,27]. However, this approach needs further investigation.

On the other hand, researchers studied the thermomechanical behaviour of tool steels in moulds. Their work extensively models heat transfer, evaluates stress [28,29] or even, estimates lifetime [29]. If straightforward transfer is impossible, several approaches for durability assessment were proposed for other industrial systems (see, for instance: [30]). In the case of moulds, Starling re-uses the Coffin–Manson equation, to qualitatively describe the thermal fatigue behaviour of nitrided steel [31]. Similar laws were proposed to describe the isothermal fatigue of coated materials [32–34], which suggests to re-use them extensively for the thermal fatigue of surface treated materials.

In this paper, a surface multi-treatment is studied for thermal fatigue resistance both experimentally and theoretically. It consists of (i) a steel boriding treatment of the substrate; (ii) a plasma-sprayed NiCrAlY bond coat; (iii) a plasma-sprayed yttria-stabilised zirconia (YSZ) as a thermal barrier coating. The results are compared with simply borided steel as well as uncoated steel, and discussed with the performance index described in [35], where the Coffin–Manson equation for fatigue was adapted for thermal fatigue resistance. The aims are: (i) to assess the new surface multi-treatment; (ii) to provide a tool to better understand thermal fatigue tests for surface treated materials; (iii) to validate a method to rank materials with respect to thermal fatigue resistance.

2. Materials and methods

2.1. Materials

After proper conditioning, annealed H13 hot work tool steel bars (diameter = 1 cm, normalised state: 1 h at 850 °C, measured hardness: 87 Rockwell B) were pack-borided at 900 °C, as described in [35]. Some of the borided bars were then sand blasted and plasma sprayed at Advanced Coatings, Liège, Belgium.

* Corresponding author. Tel.: +32 2 650 30 28; fax: +32 2 650 27 86.
E-mail addresses: pdans@ulb.ac.be (P. D'Ans), jdille@ulb.ac.be (J. Dille), mdegrez@ulb.ac.be (M. Degrez).

0257-8972/$ – see front matter © 2010 Elsevier B.V. All rights reserved.
doi:10.1016/j.surfcoat.2010.11.054

Table 1
Characteristics of the studied materials.

Materials	Metallic content (EDX, weight %)	Phase content (XRD)	Granulometry: maximum of the volumic distribution (μm)
Boriding pellets	–	Silicon carbides, B_4C, avogadrite (KBF_4)	
Pellets after boriding		Silicon carbides	
Boriding layer		Fe_2B	
NiCrAlY powder	Ni 70 – Cr 24 – Al 5 – Y 1	β-NiAl, γ-nickel (Cr in substitution)	≈65
YSZ powder	Zr 91 – Y 9	Zirconia: monoclinic, tetragonal, cubic	≈40
YSZ coating		Zirconia: tetragonal	

NiCrAlY and YSZ powders (respectively Praxair Ni-164-2 and Amdry 6643) were dried at 60 °C. Coatings were deposited in a Plasma Technik AG chamber, by rotating the samples in front of the spray device.

2.2. Characterisation and testing

The powders were analysed using a Malvernsizer S® (Malvern). A custom-made thermal fatigue tester was used: an induction coil connected to a power generator (25 kW, 63 kHz). According to a predefined program, a piston raised the sample within the coil for heating and lowered it into cold water for cooling. The samples were kept rotating to homogenise their surface temperature, which was monitored with a two-band pyrometer during heating. The tests were repeated until superficial cracks appeared and the total number of thermal cycles was considered as the lifetime. The same thermal fatigue test was successfully applied to untreated steel (with the same heat treatment), borided steel and for the overall "multi-layer". In order to further model the thermal cycles, one evaluated the heat transfer coefficient at the sample surface by measuring the temperature vs. time, starting from a preheated rotating sample.

Scanning electron microscopy (SEM) and energy-dispersive X-ray spectroscopy (EDX) were used to characterise the powders for thermal spray, cross-sections of the layers and *post-mortem* samples. Additional etchings, with Vilella's reactant were done, to reveal the steel microstructure. The bulk porosity of the plasma sprayed layers was evaluated using an image analyser software (Omnimet Advantage ®).

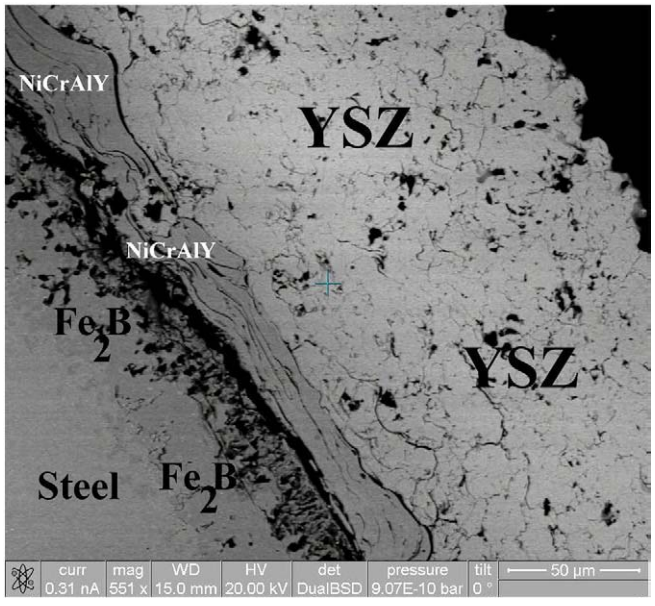

Fig. 1. SEM cross-section of the multi-layer (backscattered electrons mode).

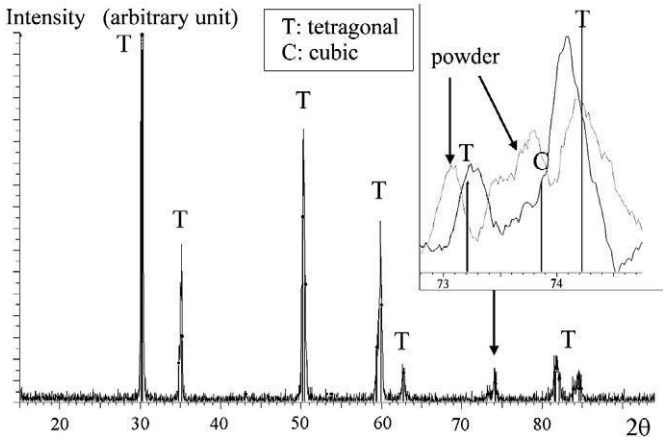

Fig. 2. X-ray diffraction of the layer; zoom: comparison with the initial powder.

The material phases were determined on additional samples via X-ray diffraction (Brücker D5000 diffractometer). Stress evaluation of the YSZ layers was based on the "two-exposure method", described by Cullity [36]. If ψ is the angle between the diffracting plane and the normal to the surface, and if d_n and d_i are the measured interplanar spacings for $\psi = 0$ and $\psi \neq 0$ respectively, the normal stress in any direction ϕ in the surface is given by:

$$\sigma_\phi = \frac{E}{(1+\upsilon)\, sin^2\psi}\left(\frac{d_i - d_n}{d_n}\right),$$

where E is the Young's modulus and υ is the Poisson's modulus [36]. In this work, two values of ψ were used (45 and 60°). The method was applied to the peaks corresponding to $2\theta = 116.1$ and 144.355°.

3. Results

3.1. Characterisation

Table 1 specifies the base materials used. The steel substrate consisted of a ferrite matrix with dispersed carbides.

A SEM cross-section of the multi-layer is given in Fig. 1. An X-ray diffractogram of the layer can be found in Fig. 2. The initial powder is a mix of the cubic and tetragonal phases (see zoom). After the plasma spray process, the cubic phase disappears.

In fact, the plasma process increased the powder homogeneity. According to the zirconia–yttria pseudo binary phase diagram [37], the cubic phase grows by reducing the "extreme" phases in terms of yttrium content (monoclinic and tetragonal) [37].

The average thickness of the layers is about 150 μm, 20 μm and 40 μm for the YSZ, NiCrAlY and boriding layers, respectively. The low boride thickness can be assigned to the high amount of alloying elements of the H13 steel, especially Mo, as well as to the carbon

Table 2
Peak shifts in the YSZ coating and biaxial stress. The interplanar spacings are calculated from the peak gravity centre.

2θ(peak position)(°) if $\psi = 0$	d_n (Angström)	ψ (°)	d_i (Angström)	σ/E (calculated)
116.1	0.90783	45	0.90743	$-9\ 10^{-4}$
144.355	0.80913	45	0.80907	$-2\ 10^{-4}$
144.355	0.80913	60	0.80923	$2\ 10^{-4}$

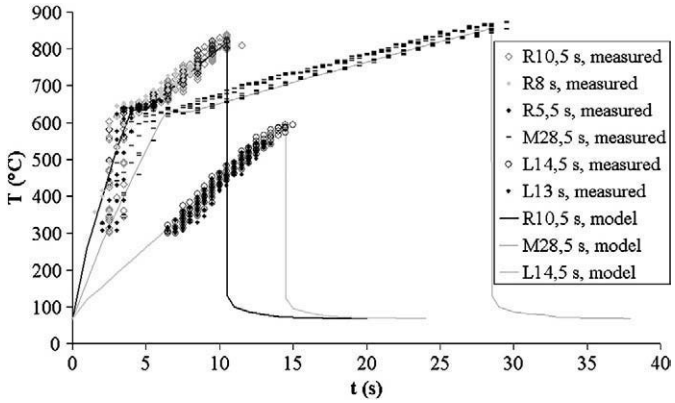

Fig. 3. thermal cycles for untreated H13 samples. Dots: pyrometer measurement; plain curves: model.

content, that both have a low solubility in Fe_2B [38]. Both the YSZ and NiCrAlY coatings have a porosity of $8{,}5 \pm 0{,}5\%$.

The biaxial ratio σ/E evaluation in the YSZ layer is detailed in Table 2. In the stress evaluation, one assumes Poissons's modulus $\upsilon = 0$, as it is typical of plasma sprayed YSZ [39]. Three measurements of σ/E were made (Table 2). They were very low and positive as well as negative. Thus σ/E barely differs from 0 statistically. Detached parts of the coating took a curvature opposite to the initial cylindrical shape of the substrate. This suggests a compressive stress at the inner side. Mechanisms explaining such a behaviour can be found in [40].

3.2. Thermal cycles description

Six types of cycles were studied. They differ by their heating powers and times. They are labelled "R", "M" or "L", for "Rapid", "Medium" and "Low" heatings, with the heating time as suffix. For instance "R10.5 s" stands for a 10.5 s rapid heating. Cooling time is 9.5 s for all studied cycles. Figs. 3 and 4 show plots of the surface temperature for all the studied cycles. Several cycles of each type are represented. The plain curves will be discussed further.

No significant difference between the plain and borided steel was observed. However, the same applied power leads to significantly lower temperature for the YSZ coated specimens.

3.3. Thermal fatigue resistance

Three failure modes were observed: a single deep crack after a low number of cycles for the most aggressive tests (Fig. 5); a shallow crack network (heat checking) for less aggressive cycles (Fig. 6); spalling of the thermal barrier coating, in the case of multi-layered specimens

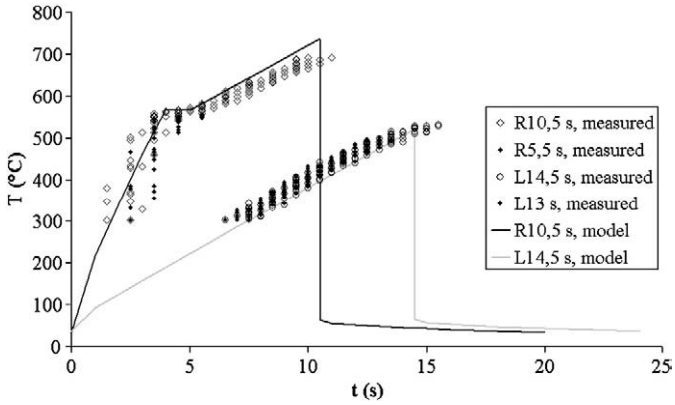

Fig. 4. Thermal cycles for the multi-layer samples.

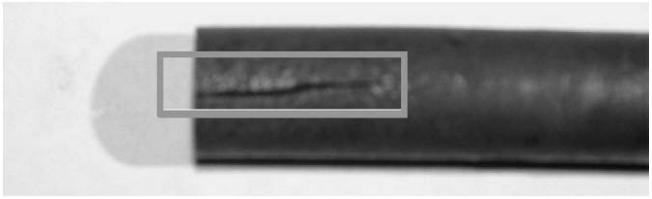

Fig. 5. Single deep crack (plain H13 steel, R10.5 s cycles).

(Fig. 7). A metallographic cross-section of the deeply cracked samples revealed the formation of martensite (Fig. 8), with an increased superficial hardness (about 600 HV, vs. 150 HV before testing). This can be attributed to the quenching effect of this thermal cycle and explains the crack morphology.

Fig. 9 gives a SEM-EDX investigation of an area that underwent spalling. The EDX spectra revealed high concentrations of iron and boron, as in the boriding layer, which indicates that the plasma sprayed layers got delaminated. Other zones have a composition similar to the NiCrAlY coating. This suggests that, on this area, the zirconia was fully delaminated and the NiCrAlY is partly delaminated.

Table 3 gives the number of cycles at failure, i.e. the number of cycles at which the abovementioned failure mechanisms occur, as well as the observed mechanism itself. When the failure is progressive, a range of cycles is given. No immediate comparison between the multi-layered and the other samples can be done, as the same power cycles lead to different observed temperature cycles. However, the low apparent resistance of the multi-layer should be pointed out. The average cooling water temperature is given in Table 4 and is used further in the modelling process.

3.4. Cooling curve for heat transfer coefficient evaluation

An uncoated sample was slowly heated to 700 °C, to ensure uniform temperature. Then, the heating was stopped and the temperature was recorded as a function of time (dots on Fig. 10). No significant difference was observed when performing the same experiment with a multi-layered sample (even if it required more power to reach 700 °C).

4. Modelling and discussion

4.1. Model

The following assumptions are made: the materials and the thermal solicitation have a cylindrical symmetry, so that no bending

Fig. 6. Heat checking (borided steel, R5.5 s cycles).

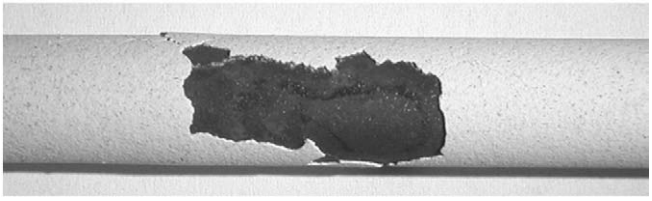

Fig. 7. Spalling of the YSZ coating (multi-layer, R5.5 s cycles).

appears; before thermal fatigue testing, the material has a uniform temperature T_0 and a biaxial stress profile $\sigma_0(x)$, inherited from the deposition processes (with a corresponding strain ε_0). Let x be the radial coordinate of the cylinder, $x=0$ being the centre. All the stress and strains are supposed to be biaxial and the heat transfer radially oriented along x.

Ranking materials with respect to thermal fatigue needs a four-step modelling:

(i) Solving the Fourier's equation with representative heat source terms, initial conditions and boundary conditions (see "data collection"). The radial thermal expansion is assumed to be negligible.

(ii) Estimating the biaxial mechanical strain at each point of the modelled material, at each time step:

$$\varepsilon_{mech}(x) \approx \varepsilon_0(x) + \varepsilon_{tot} - \alpha(x)(T(x) - T_0(x)), \quad (1)$$

where α is the thermal expansion coefficient, which is layer-dependent, $T(x)$ is the temperature profile within the stacking, ε_{tot} is the total deformation of the cylinder, resulting from the stress equilibrium of each of its components and ε_{mech} is the strain that leads to thermal stress, resulting from the difference of "length" between the free state of each material element and the "total length". In other words, ε_{mech} generates the mechanical solicitation causing thermal fatigue.

(iii) Determining extreme values of the mechanical strain during the cycles, to determine their difference $\Delta\varepsilon(x)$ and the mean stress at each element of the material, $\bar{\sigma}(x)$.

(iv) Applying the Coffin–Manson equation variants discussed in [35], which are:

$$\Delta\varepsilon_{ductile} = 3{,}5\frac{\sigma_u - \bar{\sigma}}{E} N_f^{-0{,}12} + \varepsilon_u^{0{,}6} N_f^{-0{,}6} \quad \text{(for ductile materials)} \quad (2)$$

$$\Delta\varepsilon_{brittle} = \frac{9}{4}\frac{\sigma_u - \bar{\sigma}}{E} N_f^{-0{,}083}, \quad \text{(for brittle materials)} \quad (3)$$

where σ_u is the ultimate stress, E is the Young's modulus and ε_u is the ultimate strain. In these equations, the unknown is N_f, to be determined for each x value. All the materials coefficients are also x-dependent, in presence of multiple layers. $\min_x N_f(x)$ is supposed to be the overall lifetime, since the rupture of an element of the stacking means the overall failure of the system.

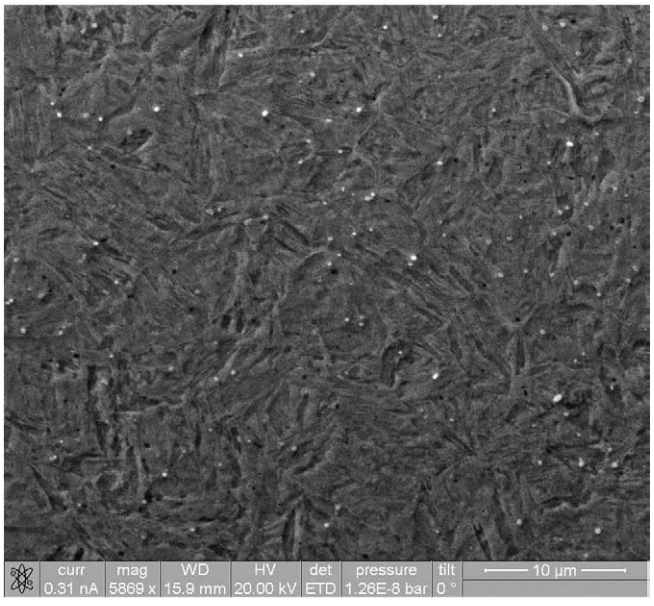

Fig. 8. Steel microstructure after the appearance of a deep single crack (R10.5 s cycles), after etching using the Vilella's reactant.

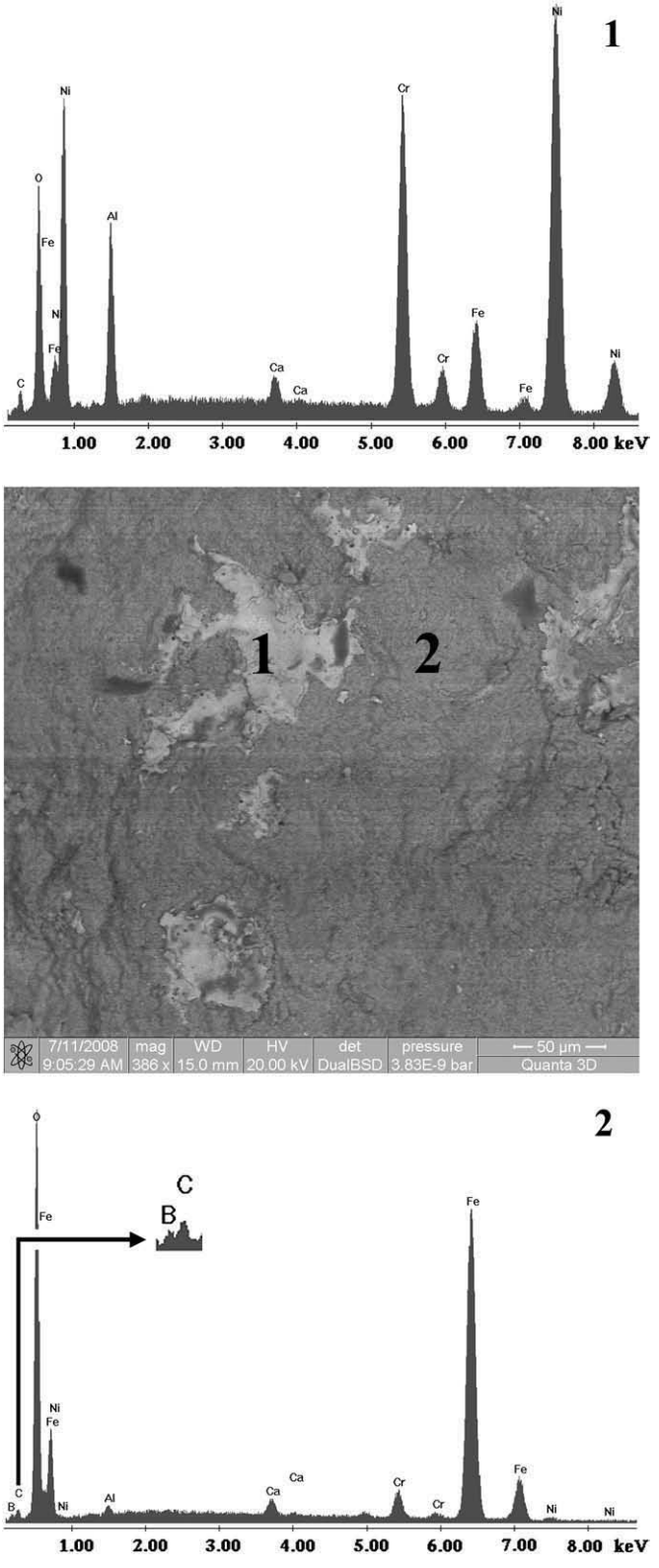

Fig. 9. YSZ spalling: SEM-micrograph (backscattered electrons) and EDX analysis.

A Matlab® code was developed to solve Eqs. (1)–(3) and to plot the related graphs. The Fourier's equation is solved for successive

Table 3
Number of cycles at failure for the studied samples and failure mode. Between brackets: failure mode: {D} = deep cracking; {H} = heat checking; {S} = spalling.

Cycles	Untreated H13	Borided H13	Multi-layer
R10.5 s	30–40 {D}	50–60 {D}	5 {S}
R8 s	180–200 {H}	120–130 {H}	–
R5.5 s	700–800 {H}	150–200 {H}	14 {S}
M28.5 s	50 {D}	–	–
L14.5 s	–	–	21 {S}
L13 s	–	–	105–110 {S}

thermal cycles, so as to obtain a limit cycle; strain profiles and lifetimes are calculated with respect to this limit cycle.

4.2. Data collection

The materials data necessary to apply this model are given in Table 5. Steel data labelled with "*" are average values on the range [25 °C; 600 °C]. The σ_0 value for Fe_2B is an assumption, based on the Young's modulus, processing temperature and Poisson's ratio of Fe_2B, as well as on the thermal expansion coefficients of both the steel and Fe_2B.

The α and $k(C_p\rho)^{-1}$ values for NiCrAlY are average values for coatings from the literature on the range [25 °C; 850 °C]. The same temperature range holds for YSZ α and C_p values. Original bulk values for C_p and ρ were adjusted to account for the measured porosity.

All the missing values are either not available in the literature, or strongly dependent on the process (like thermal conductivity for any thermal barrier coating like YSZ). Therefore, these "gaps" are filled in the next paragraphs, using the above experimental data.

The thermal loss in the air was modelled using the following boundary condition during the heating phase of the cycles:

$$-k\frac{\partial T}{\partial x}\Big|_{boundary} = h\left(T_{boundary} - T_{air}\right),$$

where the air temperature is 298 K. Solving the Fourier's equation with the same geometry (e.g. cylindrical) enables to retrieve the h value, best reproducing the air-cooling results (test described in Section 3.4) (Fig. 10). One obtains: $h = 59.3$ W/m²K. This value automatically takes the cylinder rotation into account, since the cooling experiment was performed at the same linear velocity as the thermal fatigue experiments.

Water cooling after induction heating needs the following boundary condition, to take boiling into account [41]:

$$-k\frac{\partial T}{\partial x}\Big|_{boundary} = 2,253\left(T_{boundary} - T_{water}\right)^{3,96},$$

where T_{water}, is given in Table 4.

All thermal fatigue tests start with a uniform temperature of 300 K. The internal heat source is modelled with the skin effect, due to the high frequency of the induction current. The heating curves with their particular profiles (Fig. 3), are discussed in the next paragraph.

σ_0 is set to zero for YSZ, i.e. its highest value, also observed at the outer part of the coating (Section 3.1: compressive stress inside, few stress outside), where thermal fatigue is expected to be the most detrimental. It can be shown that the mechanical properties of NiCrAlY does not influence in thermal fatigue resistance, according to the model, even if extreme values are chosen. Thus $\sigma_0 = 0$ is no bad guess.

Table 4
Average water temperature during the tests from Table 3.

Materials	Multi-layer	Multi-layer	Multi-layer	Multi-layer	Others
Cycles	R10.5 s	R5.5 s	L13 s	L14.5 s	All
T_{water} (°C)	20	20	20	25	60

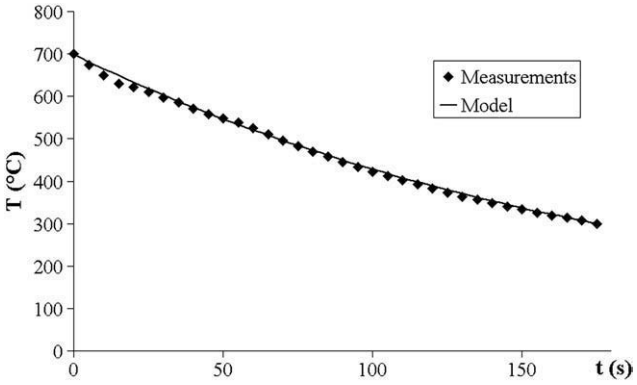

Fig. 10. Air cooling: temperature measurements and model for h.

4.3. Thermal problem

In Fig. 3, the temperature increases much slower from about 630°, because of the vicinity of the steel Curie temperature. The shape of the $T(t)$ curve is typical of steel heating [49,50] and is due to variations of several steel properties with temperature: magnetic permeability μ, electric conductivity σ and C_p [50].

Below 630 °C, the skin effect can be modelled assuming a volumic heat source of the form:

$$S(\zeta) = C_1\ exp(-2\zeta / p),$$

where p is the penetration depth defined as: $p = (\pi f \sigma \mu)^{-1/2}$ ($\approx 1.63\ 10^{-4}$ m for H13 steel), ζ is the depth from the material surface and C_1 is a constant depending on the coils geometry, the coil current and σ. Let "t^*", the heating time when the change of heating rate is observed. One has: $t^* = 4s$ in "R" cycles and 6.5 s in "M" cycles for plain steel (Fig. 3).

At higher temperatures, p strongly increases (because σ and μ suddenly change), while dT/dt at the surface strongly decreases. The temperature profile rapidly becomes flat into the material and a uniform heat source profile can be assumed: $S = C_2$.

Note that the Fe_2B magnetic properties hardly differ from those of steel [51,52]. One thus consider the boriding layer as plain steel in the thermal calculation. The temperature records are indeed similar for both cases.

Using the abovementioned Matlab code, C_1 and C_2 values were fitted, so as to obtain 630 °C after t^* and the maximum cycle temperature after the heating period for the R10.5 s and M28.5 s cycles. The calculated thermal cycles appear in Fig. 3. For the shorter cycles (like R5.5 s), it can be shown that a good agreement is obtained, reusing the same parameters values. For the "L" cycles, only C_1 was determined (as t^* is not reached, the test stops at about 600 °C).

In the case of the studied multi-layer, the same values are assumed for t^*, C_1 and C_2, but the value of k for YSZ is adjusted to match measured maximal temperatures for the L14.5 s cycles (Fig. 4). The fitted k-value is 1.1 W/mK, which is lower than the "bulk" conductivity of YSZ (>2 W/mK), as expected (plasma sprayed YSZ is indeed a porous material). Re-using the fitted parameters again leads to a good agreement for the other measured cycles (see for instance the R10.5 s cycles on Fig. 4). Note that this is only an "apparent" value, which does not allow a microscopic material description. However, it will be sufficient to evaluate the strains in the materials.

Several thermal profiles as a function of time are plotted in Fig. 11 A–D. Up to t^*, for the most rapid heating sequences, a thermal

Table 5
Data collection for interpretation and modelling. The values have different origins: redrawn from literature (followed by brackets), assumptions (like σ_0 for steel), measurements (σ_0 for YSZ), discussion or experimental fitting (see corresponding sections).

Properties	H13 steel	Fe_2B	NiCrAlY	YSZ
$C_p[J/kgK]$	608 [42] *	651 [43]	$k(C_p\rho)^{-1} =$	609 [44]
k[W/km]	30 [42] *	30 [45]	$1.70\ 10^{-6} m^2/s$	Fitted (Section 4.3)
$\rho[kg/m^3]$	7600 [42] *	7430 [45]	[44]	5582 (Section 4.2)
$\alpha[°C^{-1}]$	$13.2\ 10^{-6}$ [42] *	$8.55\ 10^{-6}$ [45]	$16.55\ 10^{-6}$ [46]	$10.67\ 10^{-6}$ [44]
$E[GPa]$	210 [47]	433	25 [39]	σ_u/E: see
$\sigma_u[MPa]$		See Section 4.5		Section 4.5
ε_u				Brittle
υ	0.30 [47]	0.30 [48]	0.25 [46]	0 [39]
$\sigma_0[GPa]$	0	−2,51	0	0 (see Section 4.5)
$x[mm]$	[0;4,96[	[4,96;5[	[5;5,02[	[5,02;5,17]

gradient appears in the material. For "slow" cycles (Fig. 11–C), no strong gradient is observed, which implies less mechanical strain into the material during heating. In multi-layer case, the calculated upper temperature is lower. The reason is that zirconia acts as a heat sink: the material is significantly thicker, and thus reaches lower temperature for the same heat amount, see Fig. 12. Note that the temperature presents a maximum under the YSZ layer. So, this thermal profile is different from that observed in real foundry conditions, where the maximum during heating is expected to be observed at the surface itself. This difference is due to the heating system choice. For this reason, this test needs a careful interpretation. However, one can expect to fit significant values of surface mechanical properties that can be used for further understanding of real conditions.

4.4. Mechanical problem

The (ε,T) cycles are plotted in Fig. 13, in which ε is the strain where it is most critical. In Fig. 13-A, the strains are taken at the outer part of the steel. The other figures show values at the outer element of each layer. In all studied cases, ε is maximum when the samples are immersed into cold water. The minimum is reached at about t^*, when the outer part of the material is compressed due to its higher temperature. The minimum value of ε depends on the heat power; in the case of steel, the negative excursion is more important for "R" cycles than for "M" cycles.

In borided steel, the steel itself exhibits a lower ε variation, because the iron boride layer slightly acts like a thermal shield (Fig. 13-B). The layer cycle is shifted toward the negative domain, because the layer was pre-stressed during its processing. The layer strain becomes tensile only when the sample is immersed into water: the underlying substrate is still hot, while the layer is cold.

Adding an YSZ coating further decreases the ε variation, for both the steel and the boriding layer. As the YSZ presents no significant initial compression on its outer surface, it experiences a large positive excursion of ε upon heating, which is detrimental for its lifetime, as observed.

This suggests modifying the deposition parameters. The cooling step generates artificially high tensile stresses affecting a material like

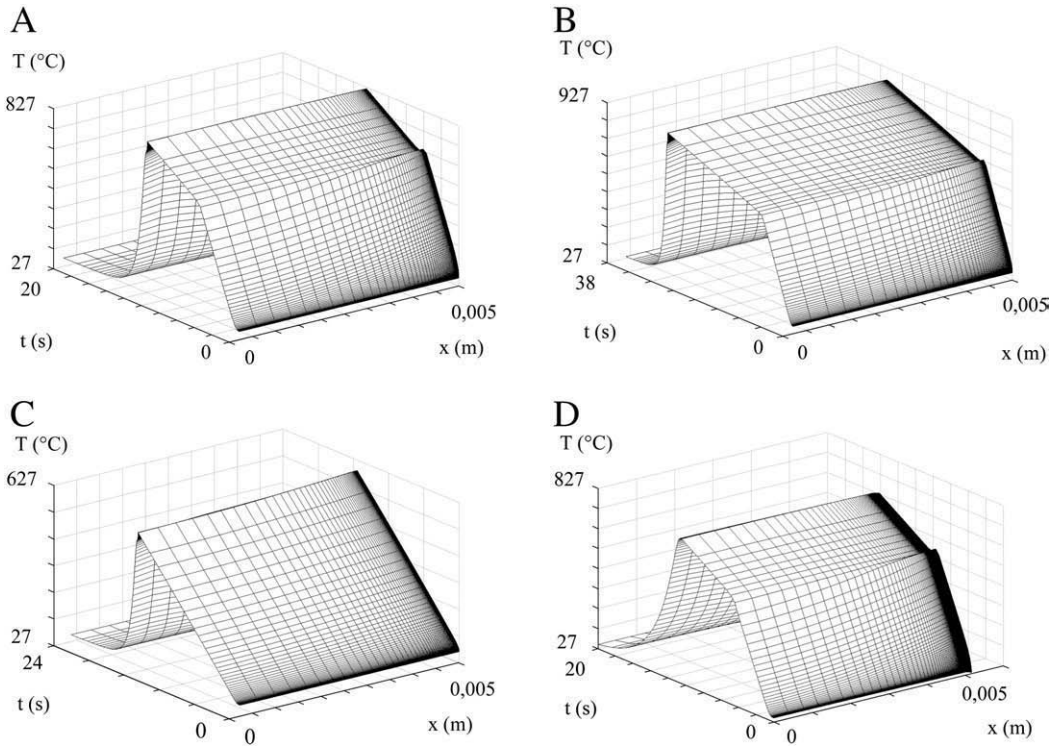

Fig. 11. thermal profile during thermal cycling: model. A) Plain steel, R10.5 s cycles. B) Plain steel, M28.5 s cycles. C) Plain steel, L14.5 s cycles. D) Multi-layer, R10.5 s cycles.

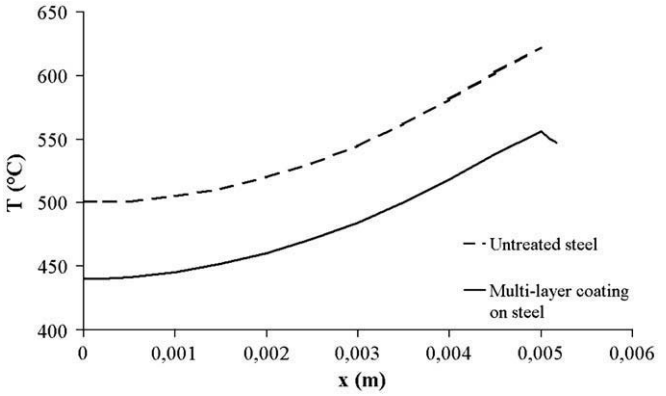

Fig. 12. Comparison of thermal profiles: plain steel vs. multi-layer, 3.7 s after starting heating, R10.5 s cycles.

YSZ. It is more severe than in real foundry conditions. Therefore, this test should not rule out such a material for this application, but rather contribute to retrieve the relevant properties for fatigue, see next section.

4.5. Lifetime, model sensitivity and model discussion

In Fig. 14, the fatigue model (Eqs. (2) and (3)) is plotted for the three studied kinds of samples. $\Delta\varepsilon$ and ε are calculated from the cycles of the previous section. For each graph, the selected materials parameters for the representation correspond to the material which limits N_f, i.e. with the smallest calculated N_f. In all cases, it corresponds to the outer layer, e.g. steel in the uncoated case, Fe_2B in the borided case and YSZ in the multi-layer case. Representative mechanical data are necessary to "fill the gaps" in Eqs. ((2) and (3)).

For quenched plain steel, σ_u and ε_u values were found in [53] for the martensitic state. For the R10.5 s and M28.5 s, cycles, martensite was rapidly formed, which explains the good agreement between the observed and calculated N_f values for those cycles (Fig. 14-A).

However, the initial material was normalised, which implies different mechanical properties. Using the relevant values ([42] and measurement of hardness combined with a conversion into σ_u [54]), a better agreement is found for the R5.5 s and R8 s cycles (Fig. 14-B).

This "transition" between ferrite and martensite also explains the brittle aspect of the fracture in the case of M28.5 s and R10.5 s cycles. Data with plain steel and Fig. 14-A and b are not sufficient to validate the model, because of this transition.

For borided steel, the $N_f = f(\bar{\varepsilon}, \Delta\varepsilon)$ was also represented (Fig. 14-C). Few σ_u and ε_u values are available for Fe_2B layers. The values from Mann for borided stainless steel are more representative of the substrate than the layer [55]. In [56], tensile tests on bulk Fe_2B are reported at different temperatures. If $550\ °C \leq T \leq 700\ °C$, $\sigma_u \approx 300 - 400$ MPa and a plastic behaviour appears. ε_u drastically varies between 1 and 7% in this range. In our work, the best fit is $\tilde{\varepsilon}_u = 2$ %. Due to the large temperature excursion in our test, we can expect that this "mean" value is fairly representative of moulds temperature in similar transients. The model is able to reproduce the facts that:

- For R5.5 s cycles, N_f is higher for plain steel than for borided steel.
- For R10.5 s cycles, N_f is higher for borided steel.

For the multi-layer system, Eq. (3) was used, since YSZ is a brittle material. A fitted value $\sigma_u/E = 0{,}61\%$ yields a good agreement (Fig. 14-D). It falls in the range mentioned in the relevant literature, even if this maximum "strain" is not necessarily evaluated from a "zero internal stress" state [37,57–59]. Owing to the relatively low testing temperatures, the possible appearance of "thermally grown oxide" is neglected. Besides, the interface defects are not explicitly modelled, so that the stresses values are "apparent" (and not local) values.

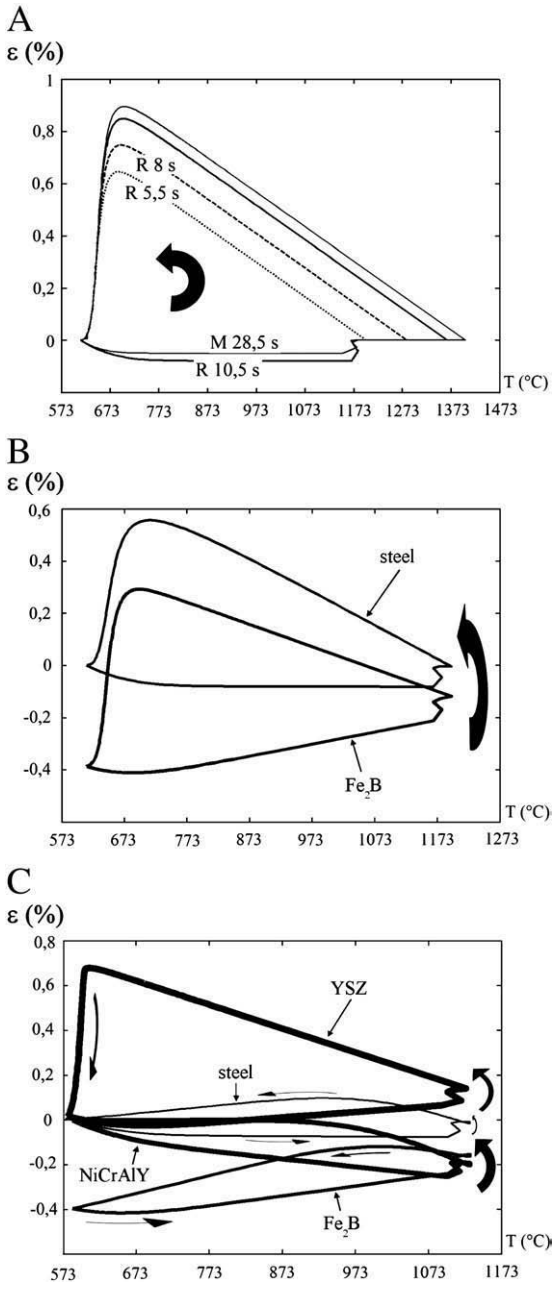

Fig. 13. Strain–temperature cycles: A) plain steel. B) borided steel (R5.5 s cycles). C) multi-layer (R5.5 s cycles).

Due to the high number of parameters, a sensitivity analysis was done. In the case of the YSZ coated samples, small changes in the values of the following parameters: α_{steel}, $(\sigma_u/E)_{YSZ}$ and $\sigma_{0,\,YSZ}$ strongly affect the calculated value of N_f, in contrast with other parameters. For instance, a 1% increase of α_{steel} affects N_f by about 20%. The model has little accuracy for brittle materials, due to the high exponent of $(\sigma_u/E)_{YSZ}$, when N_f is expressed from Eq. (3). It can then be used as a ranking tool, but not as a precise model. An improvement would be to fit a Weibull-like law to take the probabilistic character of failure into account, as a function of N_f, for a given type of cycle. Conversely, it is suggested that the fitted value of $(\sigma_u/E)_{YSZ}$ is quite accurate. It is also expected that a small decrease in $\sigma_{0,\,YSZ}$ would strongly improve N_f, which can be obtained by tuning the deposition parameters.

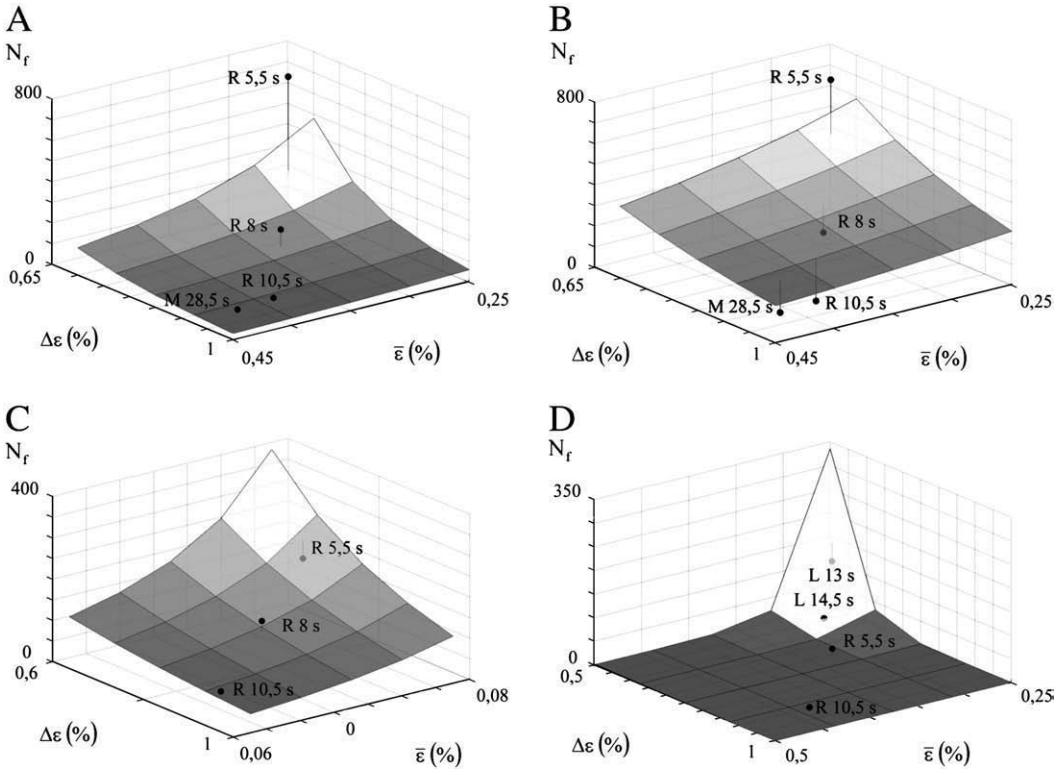

Fig. 14. Lifetime as a function of $\bar{\varepsilon}$ and $\Delta\varepsilon$: experimental and observed lifetime: A) uncoated, with martensitic steel data ($\sigma_u = 1400$ MPa, $\varepsilon_u = 0.013$ [53]) (Eq. (2)). B) uncoated, with normalised steel data ($\sigma_u = 579$ MPa,$\varepsilon_u = 0.25$[42])(Eq. (2)) C) for borided steel (Fe_2B: $\sigma_u = 400$ MPa[56], $\tilde{\varepsilon}_u = 2$ %, fitted)(Eq. (2)). D) for the multi-layer system (Eq. (3)) (YSZ: $\sigma_u/E = 0.61\%$, fitted).

5. Conclusions

An innovative multi-layer coating was synthesized and experimentally tested for thermal fatigue resistance, which turned out to be lower than for a single-treatment solution (boriding) and for plain steel.

Using these data, a thermal fatigue model was also developed and discussed. The temperature and strain profiles during the thermal cycles were simulated. The Coffin–Manson equation was adapted to evaluate the number of cycles at failure for a coated system. It successfully reproduced the well-known "S–N" curves in fatigue, while accounting for the mean stress effect, which is important in case of asymmetric thermal cycles or in the presence of non-zero deposition stresses. It also gives a better insight in understanding the test.

All thermal and mechanical coefficients of the model could be physically described. It was sometimes necessary to fit some values experimentally, but all the values remain in a physically acceptable range. However, in the case of a brittle layer, like YSZ, data are more scattered. This suggests that: (i) a statistical approach would be of interest to improve the model; (ii) tuning certain deposition parameters could strongly improve the performance of the studied multi-layer system.

Since the trends of the results can be reproduced by a Coffin–Manson like model, such an approach may be reused as a selection tool for surface treatments with respect to thermal fatigue in a given context, if the necessary properties are known and if the thermal conditions can be described.

Acknowledgements

The authors want to acknowledge: The Walloon Region of Belgium and the European Social Funding for the "First Europe" grant; Mr. Florent Campana (Advanced Coatings, Liège, Belgium) for providing samples and Professor Joris Proost (UCL, Louvain-la-Neuve, Belgium) for a useful discussion on the significance of certain plots.

References

[1] V. Joshi, A. Srivastava, R. Shivpuri, Wear 256 (2004) 1232.
[2] Z.W. Chen, Mater. Sci. and Eng., A 397 (2005) 356.
[3] V. Joshi, A. Srivastava, R. Shivpuri, E. Rolinski, Surf. Coat. Technol. 163–164 (2003) 668.
[4] N. Dingremont, E. Bergmann, P. Collignon, Surf. Coat. Technol. 72 (1995) 157.
[5] A. Molinari, M. Pellizzari, G. Straffelini, M. Pirovano, Surf. Coat. Technol. 126 (2000) 31.
[6] A. Persson, S. Hogmark, J. Bergström, Surf. Coat. Technol. 191 (2005) 216.
[7] M. Pellizzari, A. Molinari, G. Straffelini, Mater. Sci. Eng., A 352 (2003) 186.
[8] J.S. Eckersley and J. Champaigne, Shot Peening : theory and application. I.I.T.T. International, Gournay s/M., 1991.
[9] R.H. Biddulph, Thin Solid Films 45 (1977) 341.
[10] P. Hairy, R. Dussaussois, Fonderie Fondeur d'Aujourd'hui 227 (2003) 30.
[11] D.C. Lou, O.M. Akselsen, M.I. Onsøien, J.K. Solberg, J. Berget, Surf. Coat. Technol. 200 (2006) 5282.
[12] V.I. Gorokhovsky, D.G. Bhat, R. Shivpuri, K. Kulkarni, R. Bhattacharya, A.K. Rai, Surf. Coat. Technol. 140 (2001) 215.
[13] Y. Wang, Surf. Coat. Technol. 94–95 (1997) 60.
[14] C. Mitterer, F. Holler, F. Üstel, D. Heim, Surf. Coat. Technol. 125 (2000) 233.
[15] P. D'Ans, M. Bakrim, M. Brizuela, A. García-Luis, L. Segers, M. Degrez, in: MatériauxFédération Française des (Ed.), Matériaux 2006 congress, Dijon, Mise au point d'un dépôt de (Cr,Al)N par pulvérisation cathodique en vue d'applications en fonderie de l'aluminium, 2006.
[16] G. Negrea, H. Vermesan, V. Rus, International Federation for Heat Treatment and Surface Engineering, Proceedings of the 1st International Conference on Heat Treatment and Surface Engineering of Tools and Dies, PulaStudy of corrosion of chromium nitride and titanium nitride coatings in liquid aluminium, 2005.
[17] M. Pellizzari, A. Molinari, G. Straffelini, Surf. Coat. Technol. 142–144 (2001) 1109.
[18] H. Mizuno, J. Kitamura, S. Osawa, T. Itsukaichi, in: ASM Thermal Spray Society (Ed.), Proceedings of the International Thermal Spray Conference (ITSC 2005), BâleDevelopment of durable spray coatings in molten aluminum alloy, 2005.
[19] H. Mizuno, I. Aoki, S. Tawada, J. Kitamura, in: Thermal Spray Society, A.S.M. (Ed.), Proceedings of the International 2006 Thermal Spray Conference (ITSC 2006), SeattleMoB/CoCr spray coating with higher durability in molten Al and Al-Zn alloys, 2006.
[20] W.Y. Ho, D.H. Huang, L.T. Huang, C.H. Hsu, D.Y. Wang, Surf. Coat. Technol. 177–178 (2004) 172.

[21] H.J. Mathieu, E. Bergmann, R. Gras, Traité des Matériaux, Analyse et technologie des surfaces, vol. 4, Presses Polytechniques et Universitaires Romandes, Lausanne, 2003.
[22] D. Heim, F. Holler, C. Mitterer, Surf. Coat. Technol. 116–119 (1999) 530.
[23] J. Walkowicz, J. Smolik, K. Miernik, J. Bujak, Surf. Coat. Technol. 97 (1997) 453.
[24] K.S. Klimek, H. Ahn, I. Seebach, M. Wang, K.T. Rie, Surf. Coat. Technol. 174–175 (2003) 677.
[25] M. Sokovic, P. Panjan, R. Kirn, J. Mat. Proc. Technol. 157–158 (2004) 613.
[26] A. Srivastava, V. Joshi, R. Shivpuri, R. Bhattacharya, S. Dixit, Surf. Coat. Technol. 163–164 (2003) 631.
[27] T. Yasuda, A. Banno, T. Ito, K. Kiyoshi and K. Ishibayashi, Thermal spraying composite material containing molybdenum boride and a coat formed by thermal spraying (US patent 6238807), 2001.
[28] A. Persson, S. Hogmark, J. Bergström, J. Mat. Proc. Technol. 152 (2004) 228.
[29] A. Srivastava, V. Joshi, R. Shivpuri, Wear 256 (2004) 38.
[30] A. Strawbridge, H.E. Evans, Eng. Fail. Anal. 2 (1995) 85.
[31] C.M.D. Starling, J.R.T. Branco, Thin Solid Films 308–309 (1997) 436.
[32] E.S. Puchi-Cabrera, F. Martínez, I. Herrera, J.A. Berríos, S. Dixit, D. Bhat, Surf. Coat. Technol. 182 (2004) 276.
[33] Y.L. Su, S.H. Yao, C.S. Wei, W.H. Kao, C.T. Wu, Thin Solid Films 338 (1999) 177.
[34] C.M. Suh, B.W. Hwang, R.I. Murakami, Mater. Sci. Eng., A 343 (2003) 1.
[35] P. D'Ans, C. Bondoux, C. Degrandcourt, M. Bakrim, J. Dille, L. Segers, M. Degrez, Mat. Sci. Forum 595–598 (2008) 941.
[36] B.D. Cullity, Elements of X-ray diffraction, Addison-Wesley, Reading (MA), 1978.
[37] ASM, ASM Handbook online, http://products.asminternational.org/hbk/index.jsp, (last access: July 2008).
[38] A.G.v. Matushka, Boronizing, Carl Hansen Verlag, Heyden & Son, Munich-Vienne, Philadelphie, 1980.
[39] T. Lauwagie, K. Lambrinou, S. Patsias, W. Heylen, J. Vleugels, NDT&E International 41 (2008) 88.
[40] D.S. Rickerby, G. Eckold, K.T. Scott, I.M. Buckley-Golder, Thin Solid Films 125 (1987) 125.
[41] J.P. Holman, Heat Transfer, McGraw-Hill, New-York, 1989.
[42] Orvar Supreme - Hot Work Tool Steel, Uddeholm, Vienna (technical note).
[43] I. Barin, O. Knacke, O. Kubaschewski, Thermochemical properties of inorganic substances: supplement, Springer-Verlag, Berlin, New-York, 1977.
[44] K.A. Khor, Y.W. Gu, Thin Solid Films 372 (2000) 104.
[45] H.-J. Hunger, Boronizing to produce wear-resistant surface layers, Bortec GMBH, Gerlinden (technical note).
[46] S.V. Raj, L.J. Ghosn, C. Robinson, D. Humphrey, Mater. Sci. Eng., A 457 (2007) 300.
[47] MatWeb (division of Automation Creations (ACI)), MatWeb (database), www.matweb.com,(last access: July 2008).
[48] T. Endo, M. Kawakami, Zairy 32 (1983) 114.
[49] S. Zinn, S.L. Semiatin, Elements of induction heating, ASM, Metals Park, 1988.
[50] V. Rudnev, D. Loveless, R. Cook, M. Black, Handbook of Induction Heating, CRC Press, Londres, 2002.
[51] R.M. Bozorth, Ferromagnetism, Van Nostrand, New-York, 1951.
[52] S. Chikazumi, Physics of ferromagnetism, Clarendon Press, Oxford, 1997.
[53] K.S. Kim, K.M. Nam, G.J. Kwak, S.M. Hwang, International Journal of Fatigue 26 (2004) 683.
[54] GordonEngland, Hardness conversion table, http://www.gordonengland.co.uk, (last access: July 2008).
[55] B.S. Mann, Wear 208 (1997) 125.
[56] H. Taga, H. Yoshida, Met. Sci. 8 (1974) 222.
[57] V. Teixeira, M. Andritschky, D. Stöver, NATO ASI Series, Series 3, High Technology 4 (1998) 393.
[58] A.M. Limarga, S. Widjaja, T.H. Yip, Surf. Coat. Technol. 197 (2005) 93.
[59] Y.C. Zhou, T. Tonomori, A. Yoshida, L. Liu, G. Bignall, T. Hashida, Surf. Coat. Technol. 157 (2002) 118.